Tracking Li atoms in real-time with ultra-fast NMR simulations

Angela F. Harper,[1] Tabea Huss,[1] Simone S. Köcher,[2, 1] and Christoph Scheurer[1]

[1] *Fritz-Haber Institute of the Max Planck Society, Berlin (DE)*

[2] *Institut für Energie und Klimaforschung (IEK-9), Forschungszentrum Jülich GmbH, Jülich, (DE)*

We present for the first time a multiscale machine learning approach to jointly simulate atomic structure and dynamics with the corresponding solid state Nuclear Magnetic Resonance (ssNMR) observables. We study the use-case of spin-alignment echo (SAE) NMR for exploring Li-ion diffusion within the solid state electrolyte material Li_3PS_4 (LPS) by calculating quadrupolar frequencies of ^7Li. SAE NMR probes long-range dynamics down to microsecond-timescale hopping processes. Therefore only a few machine learning force field schemes are able to capture the time- and length scales required for accurate comparison with experimental results. By using a new class of machine learning interatomic potentials, known as ultra-fast potentials (UFPs), we are able to efficiently access timescales beyond the microsecond regime. In tandem, we have developed a machine learning model for predicting the full ^7Li electric field gradient (EFG) tensors in LPS. By combining the long timescale trajectories from the UFP with our model for ^7Li EFG tensors, we are able to extract the autocorrelation function (ACF) for ^7Li quadrupolar frequencies during Li diffusion. We extract the decay constants from the ACF for both crystalline β-LPS and amorphous LPS, and find that the predicted Li hopping rates are on the same order of magnitude as those predicted from the Li dynamics. This demonstrates the potential for machine learning to finally make predictions on experimentally relevant timescales and temperatures, and opens a new avenue of NMR crystallography: using machine learning dynamical NMR simulations for accessing polycrystalline and glass ceramic materials.

I. INTRODUCTION

Probing dynamical effects is particularly important for energy materials, in which mobile ions drive the device functionality. The mobility of species and structural features such as disorder and defects are closely interwoven, and often are the critical factors for determining device performance. In order to establish a correlation between structure and dynamics, various experimental ssNMR methods can be employed [1, 2]. One such method is SAE NMR, which is commonly used to study Li dynamics *in operando* within solid-state Li-ion battery materials [3–6]. SAE probes the quadrupolar interaction of the EFG tensor at the ^7Li nucleus (spin $I = 3/2$) with its local surrounding environment in order to observe the motion of Li-ions hopping between various sites in a material.

Combining *static* experimental ssNMR spectra with first principles density functional theory (DFT) is already an established method for elucidating structure in crystalline and amorphous battery materials [7–11]. Yet, up to now, this field has placed a strong focus on calculating chemical shielding (CSA) tensors, and a less prominent focus on calculating EFG tensors, mainly as quadrupolar interactions are only observed for nuclei with $I > 1/2$. While the calculation of static EFG tensors using DFT is a straightforward approach, a technique such as SAE requires computational methods that are capable of following dynamic processes over both long length and timescales. Studying these dynamics is of course impossible with DFT calculated ssNMR tensors (both CSA and EFG tensors), due to the computational constraints associated with the fact that DFT typically scales as $\mathcal{O}(N^3)$. Even recent applications of machine learning to NMR have been limited to static use-cases

[12], incapable of capturing dynamical or time-dependent effects. A classical approach using the Sternheimer approximation has proven successful for tracking ion motion in liquid electrolytes, where the fast ion motion reduces the requirements for computing NMR observables to picosecond timescales [13]. However, for slower ion motion (relative to the liquid state), this approach is not feasible, and therefore cannot be applied to study solid-state Li-ion motion, which requires simulations on the order of microseconds.

Fortunately, the recent introduction of machine learning inter-atomic potentials (MLIPs) has enabled simulations of such long-timescale processes within reasonable computational time and at sufficient fidelity for complex materials [14–16]. The first generation of MLIPs achieved speedups of three orders of magnitude over DFT, making nanosecond simulations possible in many cases [17–19]. Even more recently, a set of Ultra-Fast machine learning Potentials (UFPs) was introduced [17] which provides a speedup of nearly five orders of magnitude over DFT, while maintaining the same accuracy as some of the most accurate MLIPs such as the Gaussian Approximation Potential (GAP) [18]. With the UFP, it is now possible to routinely simulate up to the microsecond timescale almost at DFT accuracy [20–23].

By using the UFP combined with a machine learning model for EFG tensors, we can now extend the capabilities of NMR crystallography to make dynamical simulations on microsecond timescales a reality. Using this UFP+ML-EFG model, we will demonstrate how to calculate the relevant ACF of quadrupolar precession frequencies for SAE experiments in the fast ion conductor Li_3PS_4 (LPS). LPS is the ideal system to study dynamic Li processes as it has both a crystalline (β-LPS) and

amorphous (am-LPS) phase which are Li-ion conducting with predicted Li hopping mechanisms in the 10^5 to $10^7\,\mathrm{s}^{-1}$ range [24, 25]. We finally propose to use this method in combination with experimental SAE in order to further study the intermediate glass-ceramic LPS materials, which are known to have large amounts of disorder [26], as we show that SAE would be highly sensitive to understanding Li-ion motion in these materials on the micro-structural level.

II. METHODS

A. SAE NMR and the EFG tensor

SAE NMR is a probe of the change in the quadrupolar precession frequency (ω_Q) over time for a specific nucleus with a spin $I > 1/2$, such as ^{7}Li, which has a nuclear spin of $I = 3/2$. For the nucleus of a single Li atom, ω_Q is extracted from the EFG tensor $\mathbf{V}$, which describes the interaction between the quadrupole of the nucleus and its surrounding electric field. The EFG tensor is the second positional derivative of the electric field V around the nucleus,

$$V_{ij} = \frac{\partial^2 V}{\partial x_i \partial x_j} \quad . \tag{1}$$

By diagonalizing the resulting tensor and finding the eigenvalues and eigenvectors, ω_Q for each ^{7}Li atom can be computed,

$$\omega_Q = \frac{1}{2} C_Q (3\cos^2(\theta) - 1 - \eta \sin^2(\theta)\cos(2\phi)) \quad . \tag{2}$$

In Equation 2, C_Q is the quadrupolar coupling constant of a single atom of ^{7}Li, which defines the magnitude of the tensor $\mathbf{V}$, η is the asymmetry parameter which describes the shape of the tensor $\mathbf{V}$, and θ and ϕ describe the orientation of the tensor $\mathbf{V}$ with respect to an external reference system [27]. Using DFT, it is possible to calculate an individual C_Q and ω_Q for every single Li atom in the simulation. An SAE NMR experiment measures an ensemble average of the single particle correlation functions for each Li atom within different electronic environments, which have distinct ω_Q [3].

To generate an echo experimentally, which is proportional to the $\omega_Q(t)$, a Jeener Broekaert pulse-sequence is used [28, 29], and the resulting $\langle \mathrm{ACF}_{\omega_Q} \rangle$, measures the phase of $\omega_Q(t = 0)$ with $\omega_Q(t = t_m)$ where t_m is the mixing time used in the pulse sequence. In the case of $I = 3/2$ [3],

$$\langle \mathrm{ACF}_{\omega_Q} \rangle = \frac{9}{20} \langle \sin\left(\omega_Q\left(t_\mathrm{m} = 0\right) t_\mathrm{p}\right) \cdot \sin\left(\omega_Q\left(t_\mathrm{m}\right) t_\mathrm{d}\right) \rangle . \tag{3}$$

The total $\langle \mathrm{ACF}_{\omega_Q} \rangle$ is calculated as an ensemble average over all the Li sites within the sample for a given pulse time t_p, decay time t_d, and mixing time t_m. In the case

of a simulated $\langle \mathrm{ACF}_{\omega_Q} \rangle$, the pulse and decay time follow $\{t_\mathrm{p}, t_\mathrm{d}\} \to 0$, allowing us to simplify Equation 3 to [30],

$$\langle \mathrm{ACF}_{\omega_Q} \rangle \propto \langle \omega_Q\left(t_\mathrm{m} = 0\right) \cdot \omega_Q\left(t_\mathrm{m}\right) \rangle . \tag{4}$$

The $\langle \mathrm{ACF}_{\omega_Q} \rangle$ measures the probability of finding a Li-ion at time $t = t_m$ in a position with an equivalent ω_Q as it had at time $t = 0$. Thus, in materials in which the Li atoms visit sites with different ω_Q, the $\langle \mathrm{ACF}_{\omega_Q} \rangle$ in Equation 4 typically behaves as a decaying exponential function and one can extract the decay time τ_SAE directly using a stretched exponential form of the Lipari Szabo relation [3, 31],

$$\langle \mathrm{ACF}_{\omega_Q} \rangle = b^2 + (1 - b^2) \cdot \exp\left(-(t_m/\tau_\mathrm{SAE})^\gamma\right) . \tag{5}$$

The exponential Lipari Szabo decay assumes normal translational diffusion and a random orientation of the local environment with respect to the magnetic field. This assumption holds for glasses or polymer solutions which have a random distribution of environments either due to the amorphous nature of the material or due to the tumbling motion of the polymer in a liquid [13]. In an ideal liquid with fast diffusion, the stretching factor γ is 1.0, and the exponential decays to 0. However, in complex solids, some memory of previous sites may be retained during the decay and averaging might not be complete, and therefore the exponential decays to a constant value and $\gamma < 1$ occurs e.g. for cases of subdiffusion as in a diffusion-trap model [32]. From the SAE decay time, τ_SAE, the effective Li hopping rate is then given by τ_SAE^{-1}.

DFT simulations access the limit of $\{t_\mathrm{p}, t_\mathrm{d}\} \to 0$, as in Equations 4 and 5, and neglect any experimental dead time, hence allowing us to naturally simulate a non-ensemble averaged ACF_{ω_Q} for site specific trajectories within a molecular dynamics (MD) simulation. We can therefore target processes which are faster than the lower limit of what is possible in experimental SAE, as the experiment is limited by the lower bound on the order of $10\,\mu$s, defined by t_d and t_p as well as the inverse of the quadrupolar interaction [30, 33]. It is therefore possible to extract an atomistic ACF_{ω_Q} from an MD simulation as long as one can calculate the EFG tensors for all Li atoms across every snapshot of the simulation. A single snapshot of the MD simulation with ω_Q and C_Q calculated for each individual atomic site from DFT is the equivalent of the $0\,\mathrm{K}$ temperature limit, in which all motion in the system is frozen and all ions remain in their initial site. Under realistic room temperature experimental conditions for SAE, the quadrupolar observables are averaged ($\bar{C}_Q$ and $\bar{\omega}_Q$), not only over the fast timescale hopping events which are masked in experiment but also over thermal effects and different Li sites.
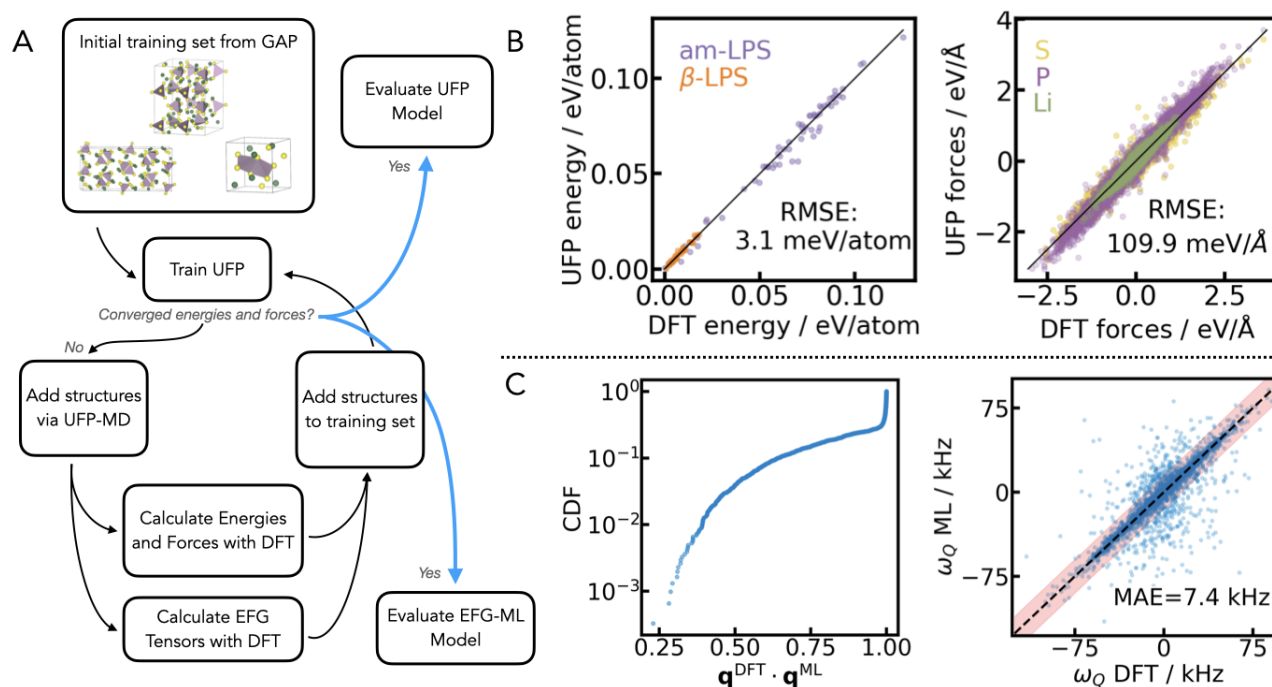
FIG. 1. **Workflow of the UFP+ML-EFG training.** The left panel shows the active learning workflow (**A**) starting from a set of structures used to train a GAP [18] for LPS [21] to the final training of the UFP (**B**) and ML-EFG model (**C**). The UFP has an RMSE in the energies of 3.1 meV/atom and forces of 109.9 meV/Å. The ML-EFG model is assessed both by the quality of the relative orientation of the tensors and the MAE in ω_Q. **C** shows the combined distribution function (CDF) of the quaternion scalar product between the DFT and ML quaternions, $\mathbf{q}^{\mathrm{DFT}} \cdot \mathbf{q}^{\mathrm{ML}}$. This indicates that the majority of tensors are oriented in the same direction comparing DFT to ML. The ML-EFG model has an error of 7.4 kHz on ω_Q, where the experimental sensitivity of ^{7}Li SAE is shown shaded in red, as 10 kHz for ω_Q.

B. UltraFast Potentials

Studying timescales relevant for spin alignment measurements necessitates an efficient methodology for the evaluation of energies and forces to drive molecular dynamics over microsecond timescales. Xie *et al.* have recently introduced a new interatomic potential, matching the accuracy of established MLIPs but boosting the speed by one or two orders of magnitude, such that it is comparable with the computational efficiency of classical force-fields [17]. The architecture uses a local representation of atomic environments as established by fundamental work using SOAP and Behler-Parinello symmetry functions [34, 35].

The energy of the system is expanded as a sum of 2-body and 3-body contributions using cubic B-splines, which combine the beneficial properties of smoothness and differentiability with the advantage of a compact support. Hence, the number of basis functions that need to be evaluated in every energy computation step is strongly limited, as a maximum of four functions can be non-zero in every segment. The low number of basis functions directly relates to a high computational efficiency [17].

The UFP is trained using the active learning procedure shown in the workflow in Figure 1A. The initial dataset is an existing set of LPS structures which was used to train

a GAP [18] for LPS [21]. The UFP is trained and iteratively improved by adding structures of β- and am-LPS to the training set. Structures are drawn from UFP-MD simulations, where the UFP used for each iteration is the most recent UFP obtained during the training workflow. This active learning cycle of training, UFP-MD simulation, and model evaluation is repeated iteratively until convergence of the UFP energy and force errors is achieved. Finally, the converged energy and force errors over a withheld test set are displayed in Figure 1B (3.1 meV/atom and 109.9 meV/Å, respectively). These are comparable with the corresponding errors for the GAP for LPS [21]. In addition to the iterative training procedure used to create a robust dataset, the hyperparameters specific to the UFP model were also optimized. Details are given in the Supporting Information Table I.

C. An ML-EFG model for EFG tensors

The Symmetry Adapted Gaussian Process Regression (SA-GPR) machine learning framework, combines covariant atomic descriptors with symmetry adapted kernels in order to learn tensors of any dimension with Gaussian process regression [36]. We have previously shown that by using tensorial learning via the SA-GPR frame-

work, we are able to predict quadrupolar frequencies (ω_Q) for the ^{7}Li nucleus within the experimental sensitivity of SAE NMR [37]. We couple the workflow for tensorial learning to the active learning procedure used for training the UFP, as shown in Figure 1A, in order to train a model for predicting the ^{7}Li EFG tensors of β- and am-LPS. The final set of structures from the active learning procedure for the UFP is used as the training set for validating the ML-EFG model.

The final set of DFT computed ^{7}Li EFG tensors over structures of Li$_3$PS$_4$ contains 166 diverse structures from the LPS UFP model, which have a total of 14,448 Li environments. The EFG tensor for each atom is calculated for all the structures using the plane-wave pseudopotential DFT code CASTEP v22 [38, 39]. The hyperparameters for the SA-GPR descriptor are optimized as described in the Supporting Information, using a 5-fold cross validation procedure with a test set, which is withheld from training. The resulting mean absolute error (MAE) for the test set in ω_Q is 7.4 kHz, and the correlation plot is shown in Figure 1C. It is important to note that the density of points of ω_Q within the red bars is high, and thus this representation highlights the outliers as they are clearer to distinguish from the majority.

In addition to evaluating the MAE in ω_Q, it is also important to validate how well the ML-EFG model predicts the orientation of the ^{7}Li EFG tensors. Besides magnitude (C_Q) and shape (η), the $\langle\text{ACF}_{\omega_Q}\rangle$ is a sensitive measure of the orientation of one tensor at a time t_m relative to another at t_0. We use the unit quaternion $\mathbf{q}$ to uniquely define the orientation of each tensor [37, 40]. The unit quaternion is a superior metric for determining orientation over Euler angles, as it is independent of the choice of reference system. Therefore, in Figure 1C, we show the cumulative distribution function (CDF) of the scalar product between the DFT calculated and ML-EFG predicted quaternions, $\mathbf{q}^{\text{DFT}} \cdot \mathbf{q}^{\text{ML}}$. A scalar product of 1 indicates perfect alignment, and from Figure 1C, we see that around 75% of the predicted EFG tensors are well-aligned with their DFT reference ($\mathbf{q}^{\text{DFT}} \cdot \mathbf{q}^{\text{ML}} \geq 0.9$). This is an important factor as it will reduce the noise in the $\langle\text{ACF}_{\omega_Q}\rangle$, Equation 4.

We finally test the ML-EFG model for size extensivity, because the system sizes included in the training set are between 200 and 256 atoms per unit cell, due to DFT performance considerations, while our target structures for β-LPS and am-LPS are 384 and 576 atoms, respectively. Therefore, we calculated the EFG tensors using DFT for two structures of β- and am-LPS each, extracted from the final 1 μs UFP simulations, and predicted the ^{7}Li EFG tensors for these four structures using the ML-EFG model (see Supplementary Information Figure S2). The accuracy of the ω_Q parameter for these four larger models is 9.2 kHz, which is below the experimentally known sensitivity of ^{7}Li SAE experiments, 10 kHz. Thus we can say with confidence that our model will have reasonable accuracy on the larger system sizes used in the final 1 μs UFP simulations.

III. RESULTS

A. Microsecond simulations with UFPs

In addition to the low energy and force errors of the UFP shown in Figure 1, it is also important to validate the behavior of the UFP relative to high quality first principles methods. Therefore, we compare the structural models generated using the UFP with literature models generated from *ab-initio* molecular dynamics (AIMD). The radial distribution function (RDF) for β-LPS and am-LPS in a 300 K, 1 μs simulation with the UFP is shown in the Supporting Information, Figure S5, in comparison with two literature references for the RDF of β- and am-LPS from AIMD [41, 42]. The UFP simulated RDFs for both β- and am-LPS show excellent agreement with AIMD. We also compare the UFP with the established method of Turbo-GAP [43] for β-LPS and am-LPS using the mean square displacement (MSD) at 500 K (see Figure S6 in the Supporting Information). We reach a perfect agreement for the am-LPS and a deviation of a factor of five for the β-LPS. The deviation can be explained with a much higher sensitivity of the MSD on the barrier height and density in the crystalline material and could potentially be improved by extending the dataset with additional nudged elastic band calculations over Li hopping events.

Furthermore, we can extract the average hopping rate of Li-ions by discretizing the MSD of all independent single ion trajectories (details of the discretization procedure are given in the Supporting Information). From the discretized trajectories we calculate Li hopping rates of 2.57×10^5 s^{-1} for β-LPS and 7.0×10^7 s^{-1} for am-LPS. Our results of significantly faster ion diffusion in am-LPS than in the crystalline β-LPS phase are in line with our previous findings and experimental reports [21, 44, 45].
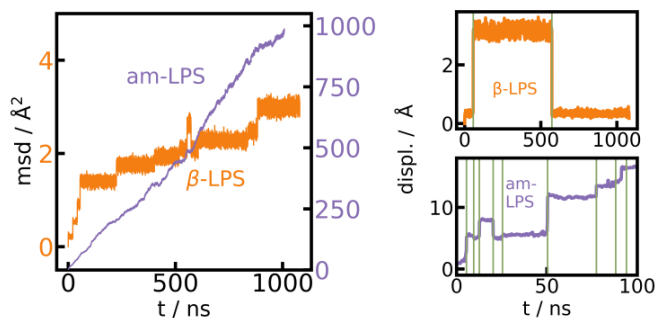

FIG. 2. **MSD for β-LPS and am-LPS using the UFP** MSD of am-LPS and β-LPS (left), showing that transport is roughly two orders of magnitude faster in the amorphous material. A showcase of hopping detection (right) from the absolute displacement in the case of β-LPS (top) and am-LPS (bottom), hops are marked with green lines.

Finally, as a result of using the UFP, we are able to simulate dynamics at 300 K for 1 μs. To the best of

our knowledge, simulations of this length have not yet been executed using MLIPs. Typical simulation times with MLIPs are on the order of nanoseconds, reaching 100 ns at most [46]. Additionally, most previous studies use higher temperatures in their MD runs [21, 47, 48], which induces an extrapolation error in their property prediction at room temperature.

With an established methodology like the Turbo-GAP, a 1 μs MD simulation would require on the order of 1 million CPUh. With an acceleration factor of 25 over Turbo-GAP, the UFP-MD for LPS on the other hand was computationally feasible in a couple of weeks (40,000 CPUh on a single compute node).

B. ACF for quadrupolar frequencies

Using the UFP+ML-EFG model, we obtain the $\langle \mathrm{ACF}_{\omega_Q} \rangle$ over a 1 μs simulation at 300 K run using the UFP for both β- and am-LPS, as shown in Figure 3. The $\langle \mathrm{ACF}_{\omega_Q} \rangle$ is averaged over all Li atoms in each system, and normalized to $[0, 1]$.
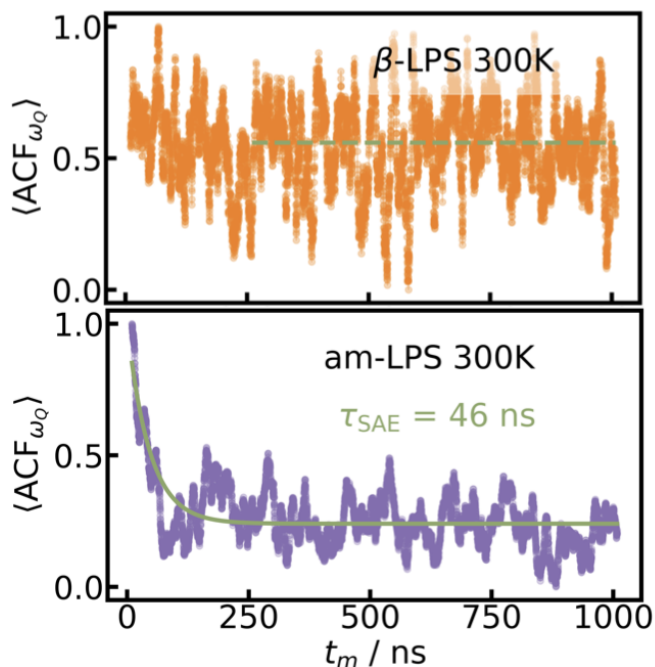

FIG. 3. $\langle \mathrm{ACF}_{\omega_Q} \rangle$ **for β-LPS and am-LPS** The $\langle \mathrm{ACF}_{\omega_Q} \rangle$ given by Equation 4 calculated over a 1 μs UFP-MD simulation at 300 K for 144 Li atoms in single-crystalline β-LPS (top, orange) and 216 Li atoms in am-LPS (bottom, purple). A decay time, $\tau_{\mathrm{SAE}} = 46$ns can be extracted from the am-LPS $\langle \mathrm{ACF}_{\omega_Q} \rangle$.

1. β-LPS

As shown in Figure 3, there is no visible decay present in the $\langle \mathrm{ACF}_{\omega_Q} \rangle$ of β-LPS at 300 K. Therefore

the $\langle \mathrm{ACF}_{\omega_Q} \rangle$ could not be fit using Equation 5. This result is expected, and occurs for two reasons.

Firstly, and perhaps most importantly, we are simulating an infinite, pristine, single crystal, by imposing periodic boundary conditions over the unit cell of β-LPS. Because SAE can only distinguish between sites with an inequivalent average local EFG [3], if Li hopping events only occur between sites with equivalent average EFGs ($\bar{\omega}_Q(t_1) = \bar{\omega}_Q(t_2)$), the $\langle \mathrm{ACF}_{\omega_Q} \rangle$ will not exhibit the characteristic exponential decay. While this would usually be associated with vanishing mobility (which is not the case in β-LPS as shown in Figure 2), it can also be due to insensitivity of SAE with respect to motion between equivalent $\bar{\omega}_Q$. Thus, if there are a few sets of mutually inequivalent sites with similar $\bar{\omega}_Q$ one would obtain a partially averaged $\bar{\omega}_Q$ [33], which is the weighted average between the $\bar{\omega}_Q$ for each of these sites. A single crystal, therefore, will always be such a case, because all of the sites have the same predominant orientation throughout the simulation. A slow decay, beyond the microsecond timescale, would be dominated in a polycrystalline material by Li motion across grain boundaries of differently oriented crystalline grains. In this case, the τ_{SAE} decay could be modeled as a function of the Li diffusion coefficient and grain size distribution.

Secondly, in this particular example of β-LPS, there are only two crystallographically inequivalent Li sites, a tetrahedral $\mathrm{LiS_4}$ site and an octahedral $\mathrm{LiS_6}$ site, which posses almost identical local EFGs. We can show this by looking at a distribution of the DFT calculated ω_Q values of all the crystalline β-LPS structures included in the training set for our ML-EFG model, shown in the left panel of Figure 4. The distributions are fairly narrow and the average $\bar{\omega}_Q$ for $\mathrm{LiS_4}$ is 10.8 kHz, and for $\mathrm{LiS_6}$ $\bar{\omega}_Q$ is 13.8 kHz, a difference of less than 4 kHz. A close look at the first 250 ns of the β-LPS $\langle \mathrm{ACF}_{\omega_Q} \rangle$ suggests that there is a small initial decay due to the inverse jump rate between $\mathrm{LiS_4}$ and $\mathrm{LiS_6}$ sites, which is undetectable due to both the signal-to-noise ratio of the $\langle \mathrm{ACF}_{\omega_Q} \rangle$ as a result of the overlap in ω_Q between the sites, as well as the low number of Li sites (144 total) in the β-LPS unit cell. This could likely be resolved in the model with a larger sampling of trajectories, but is not relevant for the observable quantities in the SAE experiment, where one would observe the residual, partially averaged coupling, shown in green.

To highlight the intricate relationship between tensor shape and orientation in β-LPS that leads to the very similar and narrow ω_Q distributions displayed in Figure 4 (left) we also compute a theoretical autocorrelation function $\langle \mathrm{ACF}_{C_Q} \rangle$ of the orientation-independent coupling constant, C_Q, experienced by the Li ions during their motion through the crystalline model in the MD simulation. We note that this is not a directly accessible quantity in the SAE experiment [49]. We compute this $\langle \mathrm{ACF}_{C_Q} \rangle$ in a similar fashion to that for ω_Q given in Equation 4,

$$\langle \text{ACF}_{C_Q} \rangle \propto \langle C_Q(t_m = 0) \cdot C_Q(t_m) \rangle \quad , \qquad (6)$$

and fit the resulting $\langle \text{ACF}_{C_Q} \rangle$ over the stretched exponential given by Equation 5 to extract a decay constant τ and Li hopping rate τ^{-1}.

A histogram of all of the individual atomistic C_Q values calculated using DFT on the β-LPS training set is shown in Figure 4, right panel. The spread of C_Q values for the LiS$_6$ sites is much wider than that for LiS$_4$, and their averages are able to be discriminated (a 30 kHz difference). LiS$_6$ sites have an average $\bar{C}_Q$ of 124.1 kHz, whereas LiS$_4$ sites have an $\bar{C}_Q$ of 90.9 kHz . Thus while $\bar{\omega}_Q$ cannot be used to distinguish these two sites, their $\bar{C}_Q$ values could be a good target to understand the local structure in ideal single crystal β-LPS.
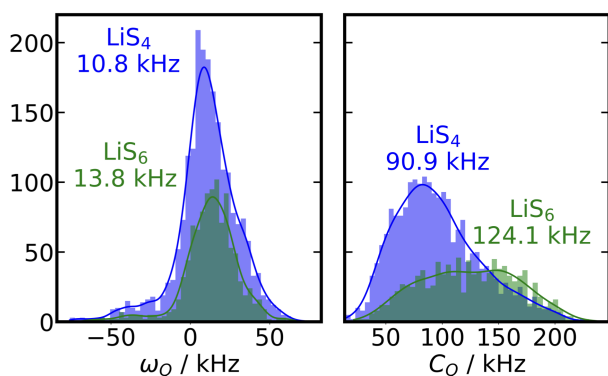
FIG. 4. **Distributions of ω_Q and C_Q in β-LPS.** The left panel shows the distribution of tetrahedral LiS$_4$ sites (blue) to octahedral LiS$_6$ sites (green), calculated using DFT, for the crystalline β-LPS structure. The right panel uses the same color scheme to show the distributions of C_Q sites for β-LPS. C_Q and ω_Q are calculated for all 33 β-LPS structures in the ML-EFG model.

Using the UFP-MD, we are able to track single-atom trajectories across the simulation, and therefore can calculate a single-atom ACF$_{C_Q}$, for each site in the β-LPS crystalline structure. In order to understand how the $\langle \text{ACF}_{C_Q} \rangle$ behaves, we separate the individual single atom ACF$_{C_Q}$, by the Li sites at time $t = 0$. In Figure 5, we plot both the individual ACF$_{C_Q}$ and $\langle \text{ACF}_{C_Q} \rangle$, where the individual ACF$_{C_Q}$ are colored by the site in which the Li atom started at time $t = 0$. The $\langle \text{ACF}_{C_Q} \rangle$ average is calculated over the 13 Li ions that experience a hop to a different site (either LiS$_4 \to$ LiS$_6$ or vice versa) during the 1 μs simulation, to reduce the noise in the $\langle \text{ACF}_{C_Q} \rangle$. We show that averaging over only the sites which hop is a reasonable assumption to make by comparing these results to a 1 μs simulation at 350 K, shown in the Supporting Information Figure S3, in which 102 Li atoms hop during the simulation, and there is better averaging over more sites.

From the top panel in Figure 5, we can clearly distinguish the individual ACF$_{C_Q}$ for LiS$_6$ sites (green), LiS$_4$

sites (blue), and hopping events between the sites, as there is a steep rise (or drop) in the ACF$_{C_Q}$ at each hopping event. Taking the average over all 13 Li sites, the $\langle \text{ACF}_{C_Q} \rangle$ does exhibit an exponential decay. Fitting the $\langle \text{ACF}_{C_Q} \rangle$ in Figure 5 to Equation 5, we find a decay time of $\tau = 1.19 \, \mu$s, or a Li hopping rate of 8.41×10^5 s^{-1}. This is on the same order of magnitude as the Li hopping rate extracted from the MSD, 2.57×10^5 s^{-1}. Additionally, by removing the orientation dependence, and averaging over only the hopping sites, we achieve better signal to noise ratio, and can more clearly distinguish the small initial decay at ($t_m < 50$ ns).

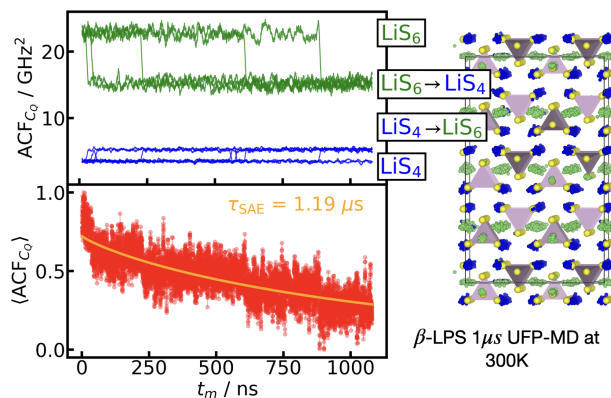FIG. 5. $\langle \text{ACF}_{C_Q} \rangle$ **for β-LPS** By considering only the Li atoms in the 300 K simulation which perform a hop to another site during the 1 μs simulation (either LiS$_4 \to$ LiS$_6$ or LiS$_6 \to$ LiS$_4$), and calculating the $\langle \text{ACF}_{C_Q} \rangle$ over these sites which hop during the simulation time we extract τ of 1.19 μs. The colors of the individual atom ACF$_{C_Q}$ shown in the top left panel correspond the starting site of the Li atom at time $t = 0$. Thus LiS$_6$ sites at $t = 0$ which hop to LiS$_4$ sites have an ACF$_{C_Q}$ in green, and LiS$_4$ sites at $t = 0$ which hop to LiS$_6$ sites are shown in blue. The trajectories of all Li atoms are colored in the same fashion in the right panel of the Li atoms trajectory.

2. am-LPS

In contrast to the β-LPS $\langle \text{ACF}_{\omega_Q} \rangle$, which exhibits no exponential decay, as shown in Figure 3, the $\langle \text{ACF}_{\omega_Q} \rangle$ for am-LPS shows a clear, fast exponential decay which can be fit to the Lipari-Szabo relation [31] given in Equation 5 ($\gamma = 1.0$). The decay time extracted from $\langle \text{ACF}_{\omega_Q}$ for am-LPS is $\tau_{\text{SAE}} = 46$ ns, which corresponds to a Li hopping rate of $\tau_{\text{SAE}}^{-1} = 2.17 \times 10^7$ s^{-1}. Comparing this with the hopping rate extracted from the MSD (7.0×10^7 s^{-1}), we see that both methods predict the same order of magnitude hopping rates for Li at 300 K. The hopping rate extracted from τ_{SAE}^{-1} is a slight underestimation to the rate extracted from the MSD, however this is consistent with the fact that the $\langle \text{ACF}_{\omega_Q} \rangle$ is not sensitive to all ion hops that occur within the material, only those for which $\omega_{t_m} \neq \omega_{t_0}$, as discussed above.

Previous work on Li hopping in LPS using a 100 ps AIMD simulation of am-LPS with 48 Li atoms at 600 K, predicts Li hopping rates in the range of 10^{11} Hz [50]. Their method for determining a Li hopping event involved tracking the escape time for Li atoms to leave a 3 Å radius surrounding the nearest polyanion and fitting this escape mechanism to an exponential decay function. Given the short timescale of the simulation, they were only able to access hopping events with residence times shorter than 100 ps (10^{10} Hz). As the shortest $\tau_{SAE} = 46$ ns, for real ion hops in am-LPS, this requires a simulation of at least several nanoseconds at 300 K considering the signal-to-noise ratio in the simulation to accurately estimate the hopping rate. This highlights the importance of simulating both at room temperature and for a sufficiently long simulation time, in order to achieve convergence of the Li dynamics and observe the correct motion of Li atoms within LPS. Similar inaccuracies from simple extrapolation to ambient conditions are expected for any material with broad and complex distributions of migration barriers that become progressively accessible upon temperature increase.

IV. DISCUSSION

This study pioneers the application of the latest generation of machine learning techniques to directly predict dynamical ssNMR observables at microsecond timescales from atomistic simulations. It is important to stress that an ssNMR calculation with DFT accuracy on the μs timescale would not be possible without leveraging machine learning to predict the EFG tensors. Calculating EFG tensors for the 576 atom am-LPS unit cell over a 1 μs simulation would cost roughly 22.5 million CPUh, with snapshots taken every 100 ps. The same prediction made using the ML-EFG model uses 500 CPUh. This is a factor of 45,000 speedup over DFT-calculated EFG tensors. Therefore, this is, to the best of our knowledge, the first dynamical ssNMR calculation performed at DFT level accuracy, and on an experimentally relevant timescale.

By integrating first-principles methodologies, it ensures consistent multi-scaling between NMR calculations derived from DFT and predictions applied to large-scale structures. Unlike AIMD studies on Li-ion conduction and diffusivity, where high temperatures are necessary in order to promote ion motion and gather enough statistics, we are able to simulate LPS at 300 K, which is the relevant temperature for comparison with realistic experimental solid state electrolyte systems.

By calculating $\langle ACF_{\omega_Q} \rangle$ in both β- and am-LPS, we find that the decay time for Li in am-LPS at 300 K is on the order of 46 ns, while the $\langle ACF_{\omega_Q} \rangle$ of single-crystalline β-LPS exhibits no characteristic exponential decay, and instead oscillates about an average value of $\langle ACF_{\omega_Q} \rangle$. By considering the orientations of the EFG tensors during the simulations in both β-LPS and am-LPS we can
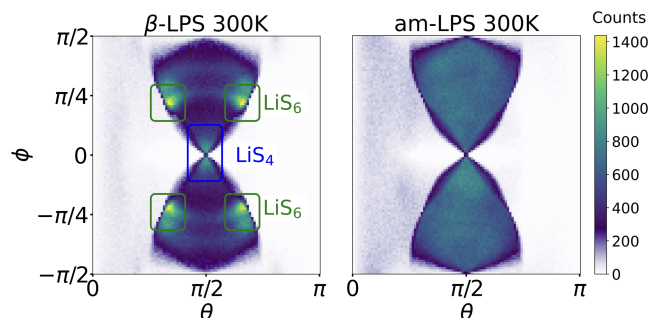

FIG. 6. **Heatmap θ and ϕ distributions in β- and am-LPS.** The heatmaps show the concentration of the angles θ and ϕ across the full 1 μs UFP-MD trajectory. The distributions are colored by the total number of sites with that combination of angles (θ, ϕ), and in β-LPS the angle pairs which arise from LiS_4 and LiS_6 sites are indicated.

see more clearly the differences in behavior of the EFG tensor in these two materials. Figure 6 shows a 2D histogram of all of the accessed angles during the full 1 μs simulation at 300 K for β- and am-LPS. In the β-LPS histogram (Figure 6 left), the majority of the angles (θ, ϕ) are clustered around either ($\pi/2$, 0) for LiS_4 tetrahedra or ($\pi/2\pm\pi/6$, $\pm\pi/4$) for LiS_6. On the other hand, there are no clear preferred values of (θ, ϕ) for am-LPS, indicating that the Li atoms experience a wide array of environments during the 1 μs simulation. The large spread in angular distribution in the am-LPS case is what leads to the characteristic rapid decay shown in Figure 3, as the Li ions visit sites with all possible orientations during the full simulation, leading to loss of correlation, which is normally characteristic of SAE in glasses or polymers [13, 51]. Once Li atoms are in a single crystalline grain, this orientational memory loss is no longer possible, and we see slow, or non existent decay as in β-LPS.

We assessed the two limits of overall microstructure in the LPS fast ion conductors. The β-LPS crystal represents an infinitely large fully uniform single crystal of LPS, as depicted in orange in Figure 7. As such, all the ω_Q values in both LiS_4 and LiS_6 sites have the same predominant value (c.f Figure 4 left), which does not vary throughout the simulation, even during Li hopping events. In addition, the mean $\bar{\omega}_Q$ for LiS_4 and LiS_6 are only 4 kHz apart, and the spread of the individual atomic ω_Q for LiS_6 is entirely contained within the distribution for LiS_4, as presented in Figure 4. Therefore, we would expect a vanishingly small decay of $\langle ACF_{\omega_Q} \rangle$ for single crystal β-LPS, in which only those two sites are accessible, and then observe a residual, partially averaged coupling throughout. However in a polycrystalline material, shown in green in Figure 7, where LiS_4 and LiS_6 sites are oriented along different crystal axes in neighboring grain boundaries, we are no longer limited by the predominant orientation of the ideal single crystal. In this case, we would expect lower τ_{SAE}, and a better sensitivity to inter-grain Li-ion motion for SAE.

At the other extreme, we consider the bulk am-LPS, represented by the unstructured purple square in Figure 7, and find that $\langle\mathrm{ACF}_{\omega_Q}\rangle$ decays rapidly over a period of 46 ns. In the homogeneous amorphous regime, we can see that as the amorphous PS_4 backbone changes across the simulation, Li atoms experience continually changing electronic environments, and thus we can think of the Li atoms moving in a "glass-like" ensemble of sites embedded in PS_4 environments. At a 46 ns decay rate, τ_{SAE} is outside of the range detectable by a real SAE experiment which would, at best, yield a small residual coupling $b > 0$ (see Equation 5). In a fast ion conductor, we expect this rapid decay of the $\langle\mathrm{ACF}_{\omega_Q}\rangle$, however this is the first time we are able to accurately quantify the rate of this decay in an amorphous material, highlighting the importance of this UFP+ML-EFG approach.

These two regimes (single crystal and fully amorphous), which are straightforward to simulate, are not representative of the realistic microstructure in glass-ceramic LPS electrolytes [26]. All of the glass ceramic materials that are critical for building the next generation of all solid state batteries such as LISICON, LIPON, LGPS, and LPS [52] lie within this range between fully amorphous to fully crystalline Li-ion conductors with hypothetical τ_{SAE} decay constants schematically depicted in Figure 7. That is, they are a mixture of glassy regions and crystalline regions (depicted as the Glass Ceramic and Polycrystalline in Figure 7), in which the Li-ion conductivity across grain boundaries is often the determining factor for the quality of these super-ionic conductors. In these cases, we propose that SAE will provide a unique grain-boundary sensitive technique for understanding Li-ion diffusion, as the intra-grain diffusion will be at either the amorphous or crystalline limit, and therefore undetectable with SAE.

Experimentally, the Grahnwehr group has observed $\tau_{SAE} \approx 30 - 50$ ms [53] in a polycrystalline sample of beta-LPS, which is well above the intra-grain decay rates we have predicted here . This can likely be rationalized by sufficiently fast ($\tau \leq 1\ \mu$s) intra-grain diffusion leading to partially averaged coupling tensors, combined with long timescale inter-grain diffusion processes between the polycrystalline grains ($\tau_{SAE} \approx$ ms). However, determining the rates and mechanisms of these processes which combine to give an experimental decay rate in the ms time scale, requires dynamical NMR crystallography and analysis techniques that allow one to unfold the various timescales and effective partially averaged interaction tensors contained in the measured data [49]. From this point onward, we now have the capability to make such an approach, by combining dynamical ssNMR with data analysis and simulations to interpret the unfolded data in terms of atomistic processes.

Beyond suggesting further work on grain-boundary simulations, we demonstrate the potential to access motion even in single pristine crystalline Li-ions, by deriving $\langle\mathrm{ACF}_{C_Q}\rangle$ and calculating a corresponding τ, which does exhibit a decay at $300\,\mathrm{K}$ for β-LPS. Furthermore,

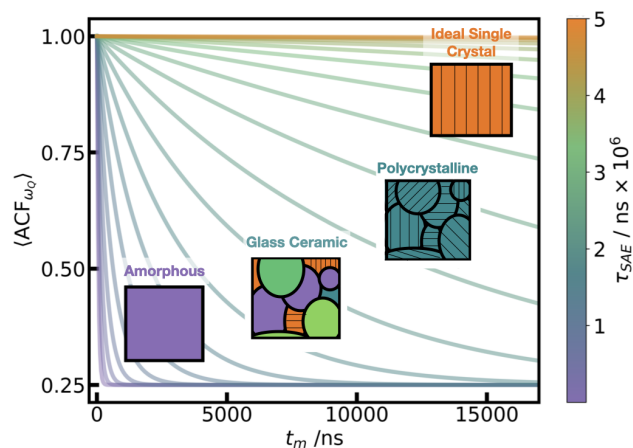FIG. 7. **Schematic of range of crystalline to amorphous** τ_{SAE} The left shows a range of decay functions, Equation 5, with τ_{SAE} from 50 ns to 5 million ns. The inset figures show schematics of the expected microscale structure at each of these varying decay rates, with black lines in the glass ceramic and polycrystalline denoting different grains.

we show that the Li hopping rate predicted by τ^{-1} from $\langle\mathrm{ACF}_{C_Q}\rangle$ is comparable with that calculated from the β-LPS MSD.

We are just at the beginning of this new era of NMR crystallography in which we are able to accurately model dynamical processes at the same temperatures and timescales as experiment. This workflow combining UFPs and experimental observables is a baseline on which the next generation of machine learning for materials methods can be based. We are now one step closer to bridging the gap between theory and experiment, and can tackle more dynamic *in operando* calculations, which were previously computationally infeasible.

AUTHOR CONTRIBUTIONS

Angela F. Harper: Data Curation, Formal Analysis, Investigation, Methodology, Visualization, Project administration, Writing - Original Draft, Writing - review and editing
Tabea Huss: Data Curation, Formal Analysis, Investigation, Visualization, Writing – Original Draft
Simone S. Köcher: Conceptualization, Supervision, Writing – review and editing
Christoph Scheurer: Conceptualization, Supervision, Funding acquisition, Writing – review and editing

CONFLICTS OF INTEREST

There are no conflicts of interest to declare.

[1] K. Märker, C. Xu, and C. P. Grey, Operando NMR of NMC811/graphite lithium-ion batteries: structure, dynamics, and lithium metal deposition, Journal of the American Chemical Society **142**, 17447 (2020).

[2] M. Gombotz and H. M. R. Wilkening, Fast Li ion dynamics in the mechanosynthesized nanostructured form of the solid electrolyte Li_3YBr_6, ACS Sustainable Chemistry & Engineering **9**, 743 (2020).

[3] M. Wilkening and P. Heitjans, From micro to macro: Access to long-range Li^+ diffusion parameters in solids via microscopic $^{6,7}Li$ spin-alignment echo NMR spectroscopy, ChemPhysChem **13**, 53 (2012).

[4] C. Yu, S. Ganapathy, E. R. v. Eck, H. Wang, S. Basak, Z. Li, and M. Wagemaker, Accessing the bottleneck in all-solid state batteries, lithium-ion transport over the solid-electrolyte-electrode interface, Nature communications **8**, 1086 (2017).

[5] K. Hogrefe, N. Minafra, W. G. Zeier, and H. M. R. Wilkening, Tracking ions the direct way: long-range Li^+ dynamics in the thio-LISICON family Li_4MCh_4 (M= Sn, Ge; Ch= S, Se) as probed by ^7Li NMR relaxometry and ^7Li spin-alignment echo NMR, The Journal of Physical Chemistry C **125**, 2306 (2021).

[6] B. Gadermaier, K. Hogrefe, P. Heitjans, and H. M. R. Wilkening, Direct assessment of ultralow Li^+ jump rates in single crystalline Li_3N by evolution-time-resolved ^7Li spin-alignment echo NMR, European Journal of Inorganic Chemistry **2021**, 1028 (2021).

[7] S. E. Ashbrook and D. M. Dawson, Exploiting periodic first-principles calculations in NMR spectroscopy of disordered solids, Accounts of Chemical Research **46**, 1964 (2013).

[8] S. E. Ashbrook and D. McKay, Combining solid-state NMR spectroscopy with first-principles calculations–a guide to NMR crystallography, Chemical Communications **52**, 7186 (2016).

[9] C. Szczuka, B. Karasulu, M. F. Groh, F. N. Sayed, T. J. Sherman, J. D. Bocarsly, S. Vema, S. Menkin, S. P. Emge, A. J. Morris, et al., Forced disorder in the solid solution Li_3P–Li_2S: a new class of fully reduced solid electrolytes for lithium metal anodes, Journal of the American Chemical Society **144**, 16350 (2022).

[10] A. F. Harper, S. P. Emge, P. C. Magusin, C. P. Grey, and A. J. Morris, Modelling amorphous materials via a joint solid-state NMR and X-ray absorption spectroscopy and DFT approach: application to alumina, Chemical Science **14**, 1155 (2023).

[11] A. F. Harper, M. L. Evans, J. P. Darby, B. Karasulu, C. P. Koçer, J. R. Nelson, and A. J. Morris, Ab initio structure prediction methods for battery materials: A review of recent computational efforts to predict the atomic level structure and bonding in materials for rechargeable batteries, Johnson Matthey Technology Review **64**, 103 (2020).

[12] M. C. Venetos, M. Wen, and K. A. Persson, Machine learning full NMR chemical shift tensors of silicon oxides with equivariant graph neural networks, The Journal of Physical Chemistry A **127**, 2388 (2023).

[13] I. Chubak, L. Alon, E. V. Silletta, G. Madelin, A. Jerschow, and B. Rotenberg, Quadrupolar $^{23}Na+$ NMR relaxation as a probe of subpicosecond collective dynamics in aqueous electrolyte solutions, Nature communications **14**, 84 (2023).

[14] V. L. Deringer, M. A. Caro, and G. Csányi, Machine learning interatomic potentials as emerging tools for materials science, Advanced Materials **31**, 1902765 (2019).

[15] T. W. Ko and S. P. Ong, Recent advances and outstanding challenges for machine learning interatomic potentials, Nature Computational Science **3**, 998 (2023).

[16] S. Batzner, A. Musaelian, L. Sun, M. Geiger, J. P. Mailoa, M. Kornbluth, N. Molinari, T. E. Smidt, and B. Kozinsky, E (3)-equivariant graph neural networks for data-efficient and accurate interatomic potentials, Nature communications **13**, 2453 (2022).

[17] S. R. Xie, M. Rupp, and R. G. Hennig, Ultra-fast interpretable machine-learning potentials, npj Computational Materials **9**, 162 (2023).

[18] A. P. Bartók, M. C. Payne, R. Kondor, and G. Csányi, Gaussian approximation potentials: The accuracy of quantum mechanics, without the electrons, Physical Review Letters **104**, 136403 (2010).

[19] I. Batatia, D. P. Kovacs, G. Simm, C. Ortner, and G. Csanyi, Mace: Higher order equivariant message passing neural networks for fast and accurate force fields, in Advances in Neural Information Processing Systems, Vol. 35, edited by S. Koyejo, S. Mohamed, A. Agarwal, D. Belgrave, K. Cho, and A. Oh (Curran Associates, Inc., 2022) pp. 11423–11436.

[20] G. Sivaraman, A. N. Krishnamoorthy, M. Baur, C. Holm, M. Stan, G. Csányi, C. Benmore, and Á. Vázquez-Mayagoitia, Machine-learned interatomic potentials by active learning: amorphous and liquid hafnium dioxide, npj Computational Materials **6**, 104 (2020).

[21] C. G. Staacke, T. Huss, J. T. Margraf, K. Reuter, and C. Scheurer, Tackling structural complexity in Li_2S-P_2S_5 solid-state electrolytes using machine learning potentials, Nanomaterials **12**, 2950 (2022).

[22] J. Zhao, J. Byggmästar, H. He, K. Nordlund, F. Djurabekova, and M. Hua, Complex Ga_2O_3 polymorphs explored by accurate and general-purpose machine-learning interatomic potentials, npj Computational Materials **9**, 159 (2023).

[23] L. C. Erhard, J. Rohrer, K. Albe, and V. L. Deringer, Modelling atomic and nanoscale structure in the silicon–

oxygen system through active machine learning, Nature Communications 15, 1927 (2024).

[24] H. Stöffler, T. Zinkevich, M. Yavuz, A. Senyshyn, J. Kulisch, P. Hartmann, T. Adermann, S. Randau, F. H. Richter, J. Janek, *et al.*, Li$^+$-ion dynamics in β-Li3PS4 observed by NMR: local hopping and long-range transport, The Journal of Physical Chemistry C 122, 15954 (2018).

[25] H. Stöffler, T. Zinkevich, M. Yavuz, A.-L. Hansen, M. Knapp, J. Bednarcik, S. Randau, F. H. Richter, J. Janek, H. Ehrenberg, *et al.*, Amorphous versus crystalline Li$_3$PS$_4$: local structural changes during synthesis and Li ion mobility, The Journal of Physical Chemistry C 123, 10280 (2019).

[26] H. Tsukasaki, S. Mori, H. Morimoto, A. Hayashi, and M. Tatsumisago, Direct observation of a non-crystalline state of Li$_2$S–P$_2$S$_5$ solid electrolytes, Scientific reports 7, 4142 (2017).

[27] P. P. Man, Quadrupole couplings in nuclear magnetic resonance, general, Encyclopedia of Analytical Chemistry 10, 9780470027318 (2000).

[28] J. Jeener and P. Broekaert, Nuclear magnetic resonance in solids: thermodynamic effects of a pair of rf pulses, Physical Review 157, 232 (1967).

[29] R. Böhmer, Multiple-time correlation functions in spin-3/2 solid-state NMR spectroscopy, Journal of Magnetic Resonance 147, 78 (2000).

[30] R. Böhmer, K. Jeffrey, and M. Vogel, Solid-state Li NMR with applications to the translational dynamics in ion conductors, Progress in Nuclear Magnetic Resonance Spectroscopy 2, 87 (2007).

[31] G. Lipari and A. Szabo, Model-free approach to the interpretation of nuclear magnetic resonance relaxation in macromolecules. 1. theory and range of validity, Journal of the American Chemical Society 104, 4546 (1982).

[32] J. C. Mauro and Y. Z. Mauro, On the prony series representation of stretched exponential relaxation, Physica A: Statistical Mechanics and its Applications 506, 75 (2018).

[33] M. F. Graf, H. Tempel, S. S. Köcher, R. Schierholz, C. Scheurer, H. Kungl, R.-A. Eichel, and J. Granwehr, Observing different modes of mobility in lithium titanate spinel by nuclear magnetic resonance, RSC Advances 7, 25276 (2017).

[34] A. P. Bartók, R. Kondor, and G. Csányi, On representing chemical environments, Physical Review B 87, 184115 (2013).

[35] J. Behler and M. Parrinello, Generalized neural-network representation of high-dimensional potential-energy surfaces, Physical Review Letters 98, 146401 (2007).

[36] A. Grisafi, D. M. Wilkins, G. Csányi, and M. Ceriotti, Symmetry-adapted machine learning for tensorial properties of atomistic systems, Physical Review Letters 120, 036002 (2018).

[37] A. F. Harper, S. Köcher, K. Reuter, and C. Scheurer, Performance metrics for tensorial learning: prediction of Li$_4$Ti$_5$O$_{12}$ nuclear magnetic resonance observables at experimental accuracy, Submitted for peer review (2024).

[38] S. J. Clark, M. D. Segall, C. J. Pickard, P. J. Hasnip, M. I. Probert, K. Refson, and M. C. Payne, First principles methods using CASTEP, Z. Kristallogr. Cryst. Mater. 220, 567 (2005).

[39] C. J. Pickard and F. Mauri, All-electron magnetic response with pseudopotentials: Nmr chemical shifts, Phys. Rev. B 63, 245101 (2001).

[40] S. W. Shepperd, Quaternion from rotation matrix, J. Guid. Control Dyn. 1, 223 (1978).

[41] M. Sadowski and K. Albe, Computational study of crystalline and glassy lithium thiophosphates: Structure, thermodynamic stability and transport properties, Journal of Power Sources 478, 229041 (2020).

[42] J. G. Smith and D. J. Siegel, Low-temperature paddlewheel effect in glassy solid electrolytes, Nature Communications 11, 10.1038/s41467-020-15245-5 (2020).

[43] M. A. Caro, Optimizing many-body atomic descriptors for enhanced computational performance of machine learning based interatomic potentials, Physical Review B 100, 024112 (2019).

[44] C. Dietrich, R. Koerver, M. W. Gaultois, G. Kieslich, G. Cibin, J. Janek, and W. G. Zeier, Spectroscopic characterization of lithium thiophosphates by XPS and XAS – a model to help monitor interfacial reactions in all-solid-state batteries, Physical Chemistry Chemical Physics 20, 20088 (2018).

[45] M. Taches, J. Malugani, R. Mercier, and G. Robert, Ionic conductivity of and phase transition in lithium thiophosphate Li$_3$PS$_4$, Solid State Ionics 14, 181 (1984).

[46] K. Shimizu, P. Bahuguna, S. Mori, A. Hayashi, and S. Watanabe, Enhanced ionic conductivity through crystallization of glass-li$_3$ps$_4$ by machine learning molecular dynamics simulations (2023).

[47] L. Gigli, D. Tisi, F. Grasselli, and M. Ceriotti, Mechanism of charge transport in lithium thiophosphate, Chemistry of Materials 36, 1482 (2024).

[48] J.-S. Kim, W. D. Jung, J.-W. Son, J.-H. Lee, B.-K. Kim, K.-Y. Chung, H.-G. Jung, and H. Kim, Atomistic assessments of lithium-ion conduction behavior in glass–ceramic lithium thiophosphates, ACS Applied Materials and Interfaces 11, 13 (2018).

[49] J. Granwehr and P. J. Roberts, Inverse Laplace Transform of Multidimensional Relaxation Data Without Non-Negativity Constraint, J. Chem. Theory Comput. 8, 3473 (2012).

[50] B. Lee, K. Jun, B. Ouyang, and G. Ceder, Weak correlation between the polyanion environment and ionic conductivity in amorphous Li–P–S superionic conductors, Chemistry of Materials 35, 891 (2023).

[51] M. Wilkening, A. Kuhn, and P. Heitjans, Atomic-scale measurement of ultraslow Li motions in glassy LiAlSi$_2$O$_6$ by two-time ^{6}Li spin-alignment echo NMR correlation spectroscopy, Physical Review B 78, 054303 (2008).

[52] Y. Wang, W. D. Richards, S. P. Ong, L. J. Miara, J. C. Kim, Y. Mo, and G. Ceder, Design principles for solid-state lithium superionic conductors, Nature materials 14, 1026 (2015).

[53] J. Granwehr, personal communication (2024).

[54] J. P. Perdew, K. Burke, and M. Ernzerhof, Generalized gradient approximation made simple, Phys. Rev. Lett. 77, 3865 (1996).

[55] G. E. Box and N. R. Draper, *Empirical model-building and response surfaces.* (John Wiley & Sons, 1987).

[56] V. Blum, R. Gehrke, F. Hanke, P. Havu, V. Havu, X. Ren, K. Reuter, and M. Scheffler, Ab initio molecular simulations with numeric atom-centered orbitals, Computer Physics Communications 180, 2175 (2009).

[57] J. P. Perdew, K. Burke, and M. Ernzerhof, Generalized gradient approximation made simple, Physical Review Letters 77, 3865 (1996).

[58] H. Jónsson, G. Mills, and K. W. Jacobsen, Nudged elastic band method for finding minimum energy paths of transitions, in *Classical and Quantum Dynamics in Condensed Phase Simulations* (World Scientific, 1998).
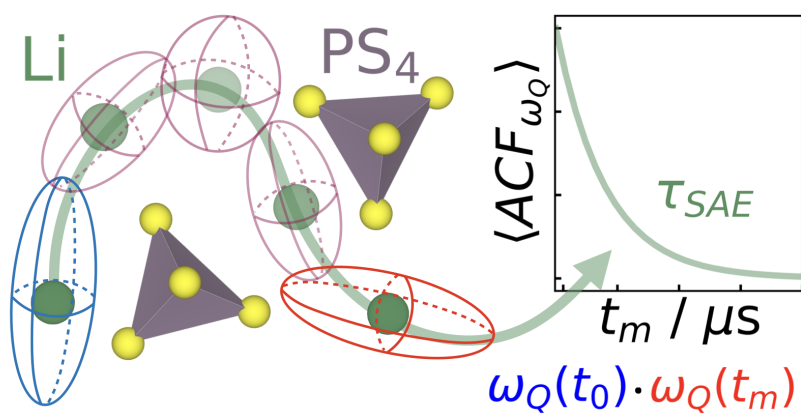
FIG. 8. **TOC Graphic** Using machine learning we are able simulate Li dynamics and predict the autocorrelation function for ^{7}Li spin alignment echo NMR in crystalline and amorphous Li$_3$PS$_4$.

Supporting Information

Appendix A: ML-EFG model hyperparameter optimization

All DFT calculations were performed with CASTEP v22.1 [38] using the C19 pseudopotential set and PBE exchange correlation functional [54]. The individual components of the EFG tensor, V_{ij}, were converged to within 4×10^{-3} V/Å^2 at a plane wave cutoff of 1200 eV and k-point spacing of $0.03 \times 2\pi \text{Å}^{-1}$. The ML-EFG approach uses λ-SOAP as the descriptor [36] which has hyperparameters l, n, r_c, and σ. These describe the number of angular components, number of radial components, cutoff radius, and Gaussian width of the descriptor. These hyperparameters were optimized using a combination of a Box-Behnken [55] design-of-experiment approach with 5-fold cross validation across a training set of 11,391 Li EFG tensors (80% of the total dataset). The optimal hyperparameters are $l = 6$, $n = 6$, $r_c = 6.0$ and $\sigma = 0.3$, which have a mean absolute error (MAE) of 7.4 kHz in ω_Q over the remaining 3057 Li environments (20% of the total data set) in the test set, which was withheld from cross validation. The MAE in C_Q and η is given in Figure S1. There is good Pearson correlation in both cases ($r > 0.85$) and low MAE (6.8 kHz MAE in C_Q and 0.99 MAE in η).
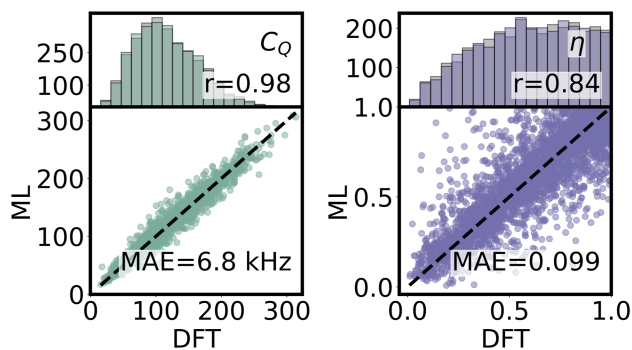

FIG. S1. **MAE over test set for C_Q and η** Histogram and correlation plot for C_Q and η evaluated over the 20% separated test set of 2057 Li environments in the ML-EFG model.

By testing the model using 11,391 Li EFG tensors on four additional large-scale structures withheld from training (results shown in Figure S2), we show that the ML-EFG model can be extended to the large LPS structures in our β-LPS and am-LPS simulations. The MAE in ω_Q over four large structures extracted from the UFP-MD trajectories is 9.2 kHz, which is within experimental accuracy of ^{7}Li SAE.
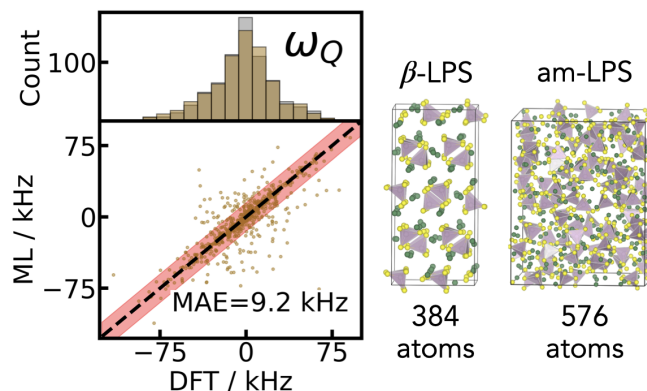

FIG. S2. **MAE in ω_Q for four large structures extracted from the UFP-MD trajectories** The left panel shows the MAE and distribution of ω_Q for a set of two β-LPS and two am-LPS structures extracted from the 1 μs UFP-MD simulations. Two of the structures are shown in the right panel, with PS$_4$ tetrahedra shown in purple (P) and yellow (S) and Li atoms shown in green.

Appendix B: Calculating autocorrelation functions

For all autocorrelation function calculations of β- and am-LPS, snapshots were extracted every 100 ps across the full trajectory. For the 1 μs calculations, this resulted in 10,000 total snapshots over which the ^{7}Li EFG tensors were predicted. The am-LPS structure has 576 atoms total with the stoichiometry Li$_3$PS$_4$, so there are a total of 216 Li atom trajectories in am-LPS over which the $\langle \text{ACF}_{\omega_Q} \rangle$ is averaged. For β-LPS there are 144 Li atoms, which $\langle \text{ACF}_{\omega_Q} \rangle$ is averaged over, and for $\langle \text{ACF}_{C_Q} \rangle$, the average is taken over only the Li ions which hop during the simulation (13 sites at 300 K and 102 sites at 350 K).

Both $\langle \text{ACF}_{\omega_Q} \rangle$ and $\langle \text{ACF}_{C_Q} \rangle$ were calculated using a sliding window averaging method in order to reduce the numerical noise between $\bar{\omega}_Q$ or $\bar{C}_Q$ at different timesteps, t_i. The sliding window average was 10 ns for $\langle \text{ACF}_{\omega_Q} \rangle$ and 1 ns for $\langle \text{ACF}_{C_Q} \rangle$. For the individual atom ACF_{C_Q} shown in Figures 5 and S3, the window was 10 ns to highlight the differences between LiS$_4$ and LiS$_6$. We can justify the validity of using the sliding window averaging through ergodicity, as averaging over a longer timescale is equivalent to averaging over a larger number of Li atoms at a fixed time. In addition, in order to account for the equilibration within the am-LPS structure, the initial $\omega_Q(t_0)$ used to reference the $\langle \text{ACF}_{\omega_Q} \rangle$ was taken as the average over the first 100 frames, or $\langle \omega_Q(t_0), \omega_Q(t_1), ... \omega_Q(t_{100}) \rangle$. Finally, the $\langle \text{ACF}_{\omega_Q} \rangle$ is normalized between $[0, 1]$.

Appendix C: Simulations at 350 K

Given the slow diffusion time in β-LPS, there are a low number of hops (13 in total out of 144 Li atoms) at 300 K, and for that reason, we have included another trajectory at 350 K for β-LPS which has 102 hops in 1 μs. The corresponding hopping rate at 350 K is 1.70×10^6 s^{-1}, as extracted from the $\langle\mathrm{ACF}_{C_Q}\rangle$ shown in Figure S3. This is an order of magnitude faster than for β-LPS at 300 K, which is the expected difference in hopping rates between these two temperatures.
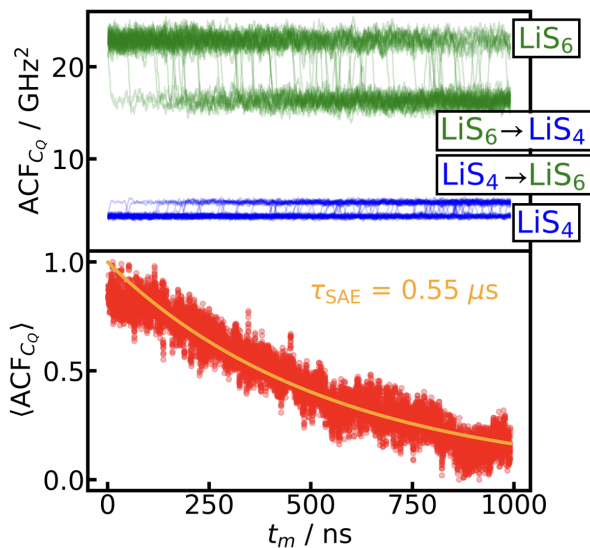

FIG. S3. $\langle\mathrm{ACF}_{C_Q}\rangle$ **for β-LPS at 350 K** The calculated $\langle\mathrm{ACF}_{C_Q}\rangle$ for a 1 μs trajectory of β-LPS at 350 K gives a decay rate of 0.59 μs or a Li hopping rate of 1.70×10^6 s^{-1}. Of the total 144 Li atoms in the cell, 102 atoms experienced a Li hopping event during the 1 μs simulation. The top panel distinguishes hopping events based on the initial site the Li atom was in at time $t = 0$. Initial LiS$_6$ sites (green) and initial LiS$_4$ sites (blue). The ACF_{C_Q} of each hopping event is labeled.

In addition to the $\langle\mathrm{ACF}_{C_Q}\rangle$ over the 1 μs simulation, we also compare the angles θ and ϕ across the different sites in β-LPS in Figure S4. In the top panel, we find that for the Li atoms which remained in their original site, the angles (θ, ϕ) were centered around $(\pi/2, 0)$ for LiS$_4$ tetrahedra and $(\pi/2\pm\pi/6, \pm\pi/4)$ for LiS$_6$. For the Li sites which experience a hopping event at some point during the 1 μs simulation, we separate these into Li-ions which started out at a LiS$_4$ and LiS$_6$ site, respectively. As expected, the distribution of angles is wider for the hopping sites than for those that do not hop, but the majority of the hopping sites are LiS$_6$ sites which hop to another LiS$_6$ site. We can see this in the LiS$_6$ hop histogram (bottom right Figure S4) which has the highest density of (θ, ϕ) at $(\pi/2\pm\pi/6, \pm\pi/4)$, which are all LiS$_6$ sites. Whereas, the LiS$_4$ hopping sites have a distribution of angles at both $(\pi/2\pm\pi/6, \pm\pi/4)$, and $(\pi/2, 0)$, indicating that some ions from LiS$_4$ sites hop into LiS$_6$

sites. However, all of these hopping events are masked in the $\langle\mathrm{ACF}_{\omega_Q}\rangle$, as in Figure 3, and are only shown here in Figure S4 by decomposing the Li trajectories by their angular components.
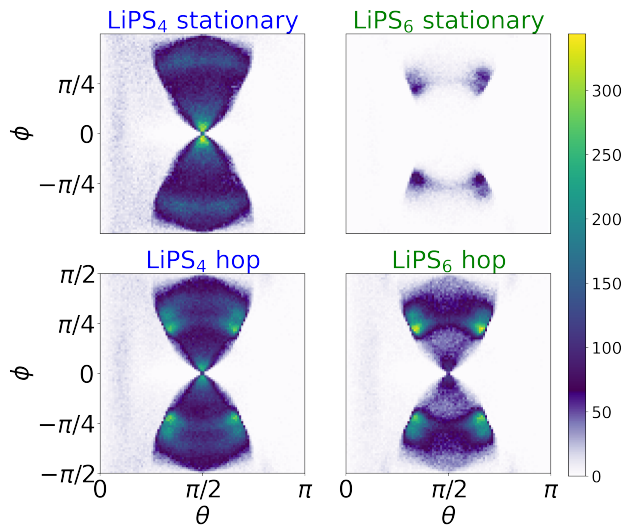

FIG. S4. **Distribution of θ and ϕ in β-LPS MD at 350 K separated by local environment.** The four heatmaps show, qualitatively, the different angular environments accessed during the 1 μs simulation for sites which do not experience a hopping event (top) and sites which do experience a hopping event (bottom) starting from either an LiS$_4$ or LiS$_6$ site. The histograms are colored by the number of Li sites across the trajectory which have a given (θ,ϕ).

Appendix D: Technical details of the UFP fitting

The UFP-MD simulations for training are executed at temperatures ranging from 300 K to 1000 K, using a time step of 2 fs, and a simulation time of either 1 ns or 1 μs in the NpT ensemble. All DFT reference calculations used for generating the UFP are performed using FHI-AIMS [56], the PBE exchange-correlation functional [57] and a $2\times2\times2$ k-point sampling. Hyperparameter optimization was performed and the results are shown in Table I. The RDFs of β-LPS and am-LPS compared to AIMD from [41, 42] are shown in Figure S5.

TABLE I. **Hyperparameters of the UFP**

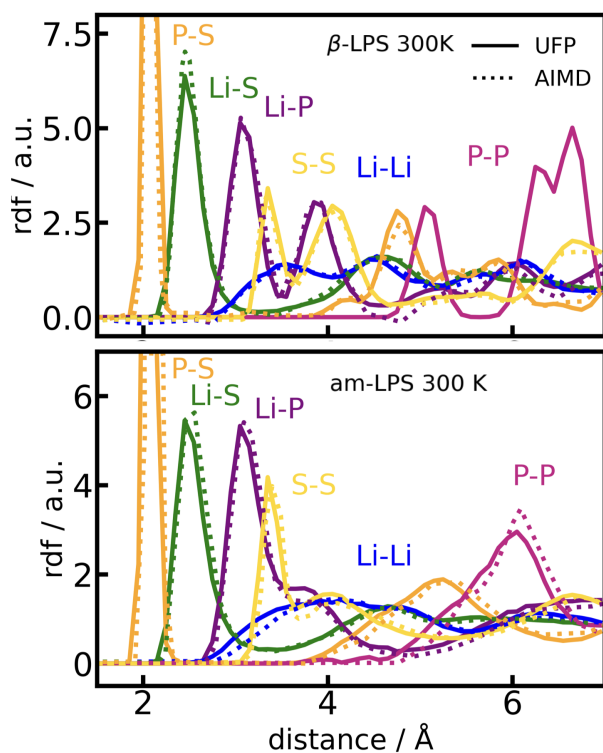| Description	2B	3B
cutoff	6 Å	5 Å
lower cutoff	1 Å	1 Å
spline distance	0.4 Å	0.4 Å
ridge regularisation	1e-5	1e-6
curvature regularisation	1e-5	1e-5
κ		0.1
leading trim		0
trailing trim		3

FIG. S5. **Radial distribution functions of β-LPS and am-LPS in comparison to AIMD references**. β-LPS (top) is compared to the AIMD RDF from Sadowski *et al.* [41] and am-LPS (bottom) to the AIMD RDF from Smith *et al* [42].

Finally, to compare the atom dynamics in the UFP versus another high quality machine learning potential for LPS, we simulated a 1 ns trajectory at 500 K for both β- and am-LPS using the UFP [17] and TurboGAP [43]. The resulting MSDs are shown in Figure S6, and we find that for am-LPS the MSD is comparable between Turbo-GAP and the UFP, and for β-LPS we have a five times faster transport in the TurboGAP compared to UFP. This can be explained by a insufficient barrier sampling in the approaches, as the fitting of the interatomic potentials is done using snapshots from MD simulations. Those snapshots are strongly biased towards the minima and a better estimate of the barrier height could be achieved by including nudged elastic band [58] trajectories from DFT into the training sets of both MLIPs.

Appendix E: Technical details of jump detection

For the discretization in order to detect jumps, we utilize a hopping classification inspired by Smith *et al.* [42],

$$h_i(t,a) = \theta(|r_i(t) - r_i(t_0)| - a)), \quad (S1)$$

where θ is the Heaviside function and a is a threshold of square displacement. We set a to 3 Å and provide a sensitivity analysis for this parameter (Figure S7). The
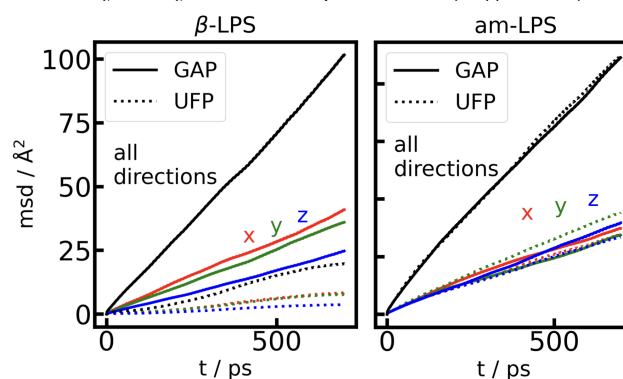

FIG. S6. **Mean square displacement of a 1 ns MD run of β-LPS and am-LPS at 500 K** The MSD for β-LPS (left) and am-LPS (right) is compared between 1 ns simulations in TurboGAP [43] and UFP [17] in order to validate the Li diffusion behavior in the UFP model.

hopping detection method, Equation S1, is run over a single Li trajectory until a hop is detected, and then repeated iteratively, using the detected hopping point as a new starting point. Also an additional filter is used which ensures a residence time of 0.5 ns to exclude jump attempts from the detection. Examples of discretized Li squared displacement trajectories of the β-LPS are shown in Figure 2b.

We test the sensitivity of the calculated jump frequency from MD simulations on the selected threshold a from Equation S1 and show the result in Figure S7. We find a plateau between 2.8 and 3.2 Å and thus select a cutoff of 3 Å.
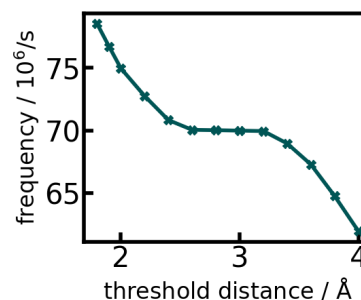

FIG. S7. **Sensitivity of the computed jump frequency on the selected threshold a of the absolute displacement for am-LPS** By varying the threshold distance, a for computing a jump frequency we find a window in which the jump frequency is stable (between 2.8 and 3.2 Å) and use this to select the optimal threshold distance, 3.0 Å.